ACS Photonics

pubs.acs.org/journal/apchd5

Article

Highly Selective Color Filters Based on Hybrid Plasmonic–Dielectric Nanostructures

Anabel De Proft,* Kristof Lodewijks, Bruno Figeys, Dmitry Kouznetsov, Niels Verellen, Nga P. Pham, Bart Vereecke, Deniz Sabuncuoglu Tezcan, Roelof Jansen, Pol Van Dorpe, and Xavier Rottenberg

Cite This: https://doi.org/10.1021/acsphotonics.1c01983

Read Online

ACCESS | Metrics & More | Article Recommendations | Supporting Information

ABSTRACT: We demonstrate a novel transmission color filter design that exploits both dielectric and plasmonic resonances to establish a highly color-selective device, reaching an experimental full-width at half-maximum (fwhm) that is only half that of previously demonstrated cost-effective color filter devices for the same peak transmission and better out-of-band rejection. The measured fwhm is only 25 nm, and the peak transmission reaches up to 53%. The filter uses the interference of Fabry-Pérot resonances and guided-mode resonances in two separated dielectric slabs to achieve this excellent fwhm while relying on propagating surface plasmon polaritons to achieve the excellent out-of-band rejection. A simulation study elucidates the nature of the optical modes in the device and their interference mechanisms and reveals the most important design considerations. Fabrication was done in a CMOS pilot line and is cost-effective, as it requires only two metal patterning steps. Fabrication imperfections are discussed, together with strategies to mitigate them. We show the correct mitigation of these imperfections leads to further performance gain, enabling a full-width at half-maximum down to 20 nm and a peak transmission beyond 60%. We believe this novel filter design is a powerful concept to improve the spectral resolution of color filters for cost-effective multispectral imaging. Beyond multispectral imaging, the design could be adapted for other applications that require on-chip spectral filtering in a thin form factor.

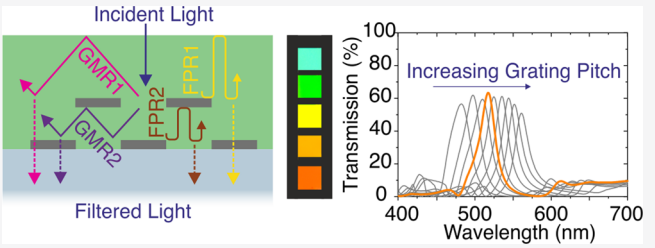

KEYWORDS: *multispectral imaging, structural color filter, plasmonics, surface-plasmon polariton, Fabry-Pérot resonance, guided mode resonance*

The ability for cameras to have color sensitivity beyond the primary colors red, green and blue, as found in most commercially available CMOS cameras, enables many applications that require more detailed spectral information. Such cameras are capable of what is known as multispectral or hyperspectral imaging, depending on the spectral resolution achieved.[1] Multispectral imaging applications include the remote sensing of terrestrial features,[2] machine vision for agricultural products,[3] and spectral biomedical imaging.[4] All-dielectric thin-film interference color filters have been integrated on top of CMOS image sensors successfully to produce cameras with up to 100 color bands in the visible, enabled by the 10 nm full-width at half-maximum (fwhm) of a single color filter (CF) passband.[5,6] They selectively transmit colors because of interference phenomena in the multilayer stack. Although these all-dielectric thin-film CFs boast excellent color selectivity and transmission efficiency, each color band requires a different stack thickness, which leads to a high number of fabrication steps to embed all color bands on one single image sensor array. Structural CFs are being investigated extensively to replace the all-dielectric thin-film CFs because of their limited thickness and limited number of fabrication steps that do not scale with the number of required color bands. They operate through interaction of light with 2D-patterned nanostructures, making the central wavelength of the transmission band tunable with only lateral geometric dimensions like the width and spacing of the nanostructures,[7−9] drastically reducing the optical path length necessary for color filtering compared to all-dielectric thin-film CFs.

Structural CFs with plasmonic nanostructures have received particular interest in recent years due to their strong enhancement of local fields, giving them the ability to interact strongly with light in very thin structures.[10] The arrayed, plasmonic nanostructures spectrally filter light because incident light excites surface plasmon resonances (SPRs), collective oscillations of free electrons in a metal coupled to the electric field in an adjacent dielectric.[11] They are generally categorized into propagating surface plasmon polaritons (SPPs) and localized surface plasmon resonances (LSPRs). SPPs are now

Received: December 23, 2021

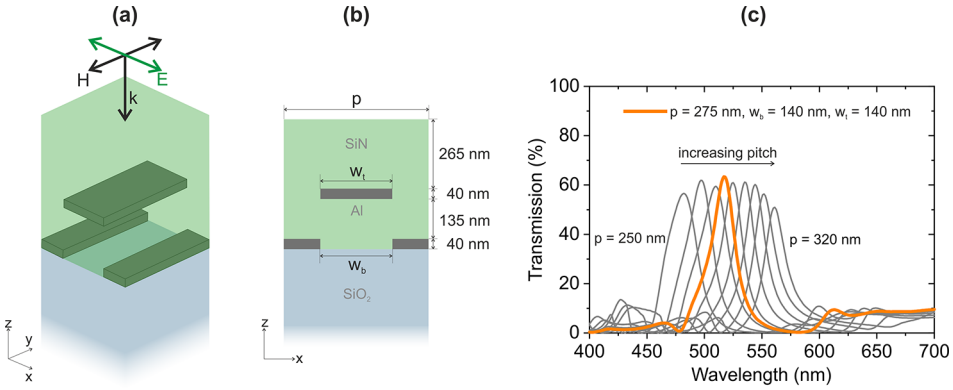

Figure 1. Novel CF unit cell design and its simulated transmission spectrum. (a) One unit cell of the CF structure with the polarization of the incident light indicated (*E* field perpendicular to the metal lines). (b) The cross-section of the CF unit cell along the *xz*-plane. The pitch *p* is varied from 250 to 320 nm. It is 275 nm for the central design. The central design has a bottom grating line width w_b of 140 nm and a top grating line width w_t of 140 nm. (c) The transmission spectra of the proposed design for increasing *p*. The transmission spectrum of the central design is highlighted in orange. The w_b and w_t for the designs with different *p* values are optimized separately on a pitch-by-pitch basis.

known to be the mechanism behind extraordinary optical transmission (EOT),[12] which is the wavelength-selective transmission of light through metallic hole arrays. EOT and other phenomena caused by SPRs present in a periodic metal hole array have been studied extensively for color filter applications,[13−16] encouraged by the cost-effective fabrication of a single-layer patterned metal sheet. A common problem for these metal hole array CFs is their rather low color selectivity compared to all-dielectric thin-film CFs, although impressively high transmission efficiencies for metal hole array CFs have been reported recently.[17] For that reason, hybrid dielectric−plasmonic CFs have been investigated[18,19] to combine the sharp dielectric resonances with the broad plasmonic resonances, resulting in experimentally demonstrated fwhms down to 45 nm for a peak transmission of 60%.[20]

We report on a novel hybrid dielectric−plasmonic CF design with a fwhm of only 25 nm and a peak transmission of 53%. Our device design consists of two stacked parallel aluminum (Al) gratings embedded in a silicon nitride (SiN) slab. The color selectivity of the CF relies on the interference of different dielectric resonances in two separate sections of the main SiN slab region, delimited by one of the Al gratings. In each of these sections, the resonances are Fabry-Pérot resonances (FPRs) and guided mode resonances (GMRs). GMRs occur when diffracted light from a grating couples to a waveguide mode,[21−23] and the concept has been used to develop all-dielectric color filters in the past.[24] In addition, propagating SPPs occur at the boundaries of the visible spectrum, suppressing the unwanted transmission outside the main color band.

In this paper, we first perform a simulation study of the device functionality with a finite-difference time-domain (FDTD) model. By separating the CF structure into separate substructures, we aim to gain better insight into the working principle of the full structure. Second, we will show the experimental results for the fabricated CFs. Finally, we will use an additional simulation study to investigate the effect of several fabrication imperfections and discuss how these imperfections can be mitigated to further decrease the fwhm down to 20 nm and increase the peak transmission beyond 60%.

RESULTS AND DISCUSSION

Color Filter Design and FDTD Simulation Results. The CF design we propose consists of two parallel Al gratings with the same pitch embedded in a SiN slab at different heights. The SiN slab is stacked on top of a SiO_2 substrate. One grating is placed directly on top of the substrate, the other grating is fully embedded in SiN. The two gratings are offset from each other along the horizontal *x*-axis by half the grating pitch. Figure 1a shows the unit cell of the proposed CF design and Figure 1b its cross-section along the *xz*-plane, together with the dimensions of the structure. The simulated transmission spectrum for a unit cell design with a pitch of 275 nm is shown in Figure 1c in orange. Spectra for different pitches are shown in gray and illustrate how the full visible spectrum can be covered. For explanatory purposes, we will focus on the pitch of 275 nm design as the central design throughout the rest of this paper. The central design shows a simulated fwhm of 20 nm, with a peak transmission of 63%. We separate the structure of this central design into substructures to isolate different plasmonic resonances, FPRs and GMRs, and investigate how these resonances are affected by key geometric parameters. We will build up the final device from these separate substructures to gain insight into the interference of the different resonances in the final structure and how this leads to the excellent fwhm and peak transmission. Details on the FDTD simulation setup can be found in Methods.

Single Metal Grating in Dielectric Medium. To comprehensively investigate the mechanisms leading to the transmission spectrum of the final design, we start by analyzing the simplified substructure containing only a single Al grating with three different configurations of dielectric substrate and superstrate. The first configuration, *sym*SiO_2, has a SiO_2 substrate and superstrate, the second configuration, *symSiN*, has a SiN substrate and superstrate, and the third configuration, *asym*, has a SiO_2 substrate and SiN superstrate. The transmission spectra for all three configurations are shown in Figure 2.

In all three configurations there are two kinds of interfaces: Al−SiO_2 and Al−SiN. Starting with the configurations that contain at least one Al−SiO_2 interface, *sym*SiO_2 and *asym*, we see they both have distinct spectral features between 400 and 450 nm. Two phenomena occur here: the Rayleigh anomaly, for both gratings at 398 nm, and the coupling of incident light

https://doi.org/10.1021/acsphotonics.1c01983
ACS Photonics XXXX, XXX, XXX−XXX

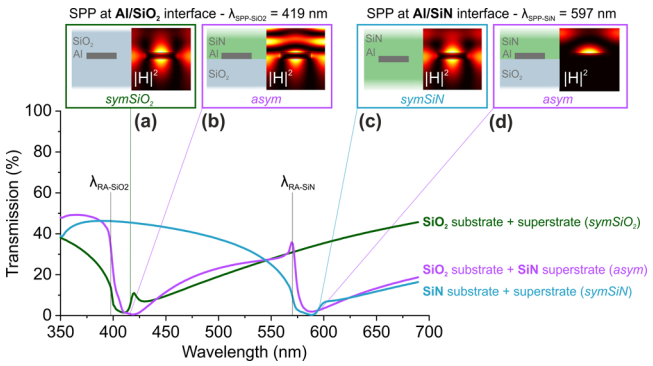

Figure 2. Investigating the transmission behavior of a single metal grating in three different dielectric configurations: *symSiO*$_2$ with a SiO_2 substrate and superstrate, *symSiN* with a SiN substrate and superstrate, and *asym* with a SiO_2 substrate and SiN superstrate. The magnetic field $|H|^2$ is shown in (a) for the SPP at the *symSiO*$_2$ top and bottom Al−SiO_2 interface, in (b) for the SPP at the bottom *asym* Al−SiO_2 interface, in (c) for the SPP at the top and bottom *symSiN* Al−SiN interfaces, and in (d) for the SPP at the top *asym* Al−SiN interface.

to SPPs, for both gratings at 419 nm. The Rayleigh anomaly $\lambda_{RA\text{-}SiO_2}$ occurs when incident light diffracts to 90°, effectively coupling into the grating (see Methods for the analytical formula). The grating-assisted coupling of incident light to SPPs occurs when the grating pitch makes up for the momentum mismatch between the SPP and incident light (see Methods for the analytical formula). For our structures, that condition is met for $\lambda_{SPP\text{-}SiO_2}$ 424 nm. For both gratings, we observe a slight blueshift to 418 nm because that is the wavelength at which the width of the grating line satisfies the $\lambda/2$ condition for a standing SPP wave on a single grating line. Although the central wavelength of SPP coupling is 418 nm for both gratings, the line shape around it appears different. That is because the *symSiO*$_2$ grating supports extraordinary optical transmission (EOT) and the *asym* grating does not. EOT describes the enhanced transmission of light through a thin metal sheet with subwavelength perforations: incident light couples to SPPs at the top interface, those SPPs propagate to the bottom interface that is identical to the top interface and from that bottom interface they are finally re-emitted. The re-emitted light interferes with directly transmitted light and a complex of destructive and constructive interference is centered around $\lambda_{SPP\text{-}SiO_2}$, as we see in the transmission spectrum for *symSiO*$_2$. The presence of SPPs at the top and bottom interface simultaneously is confirmed by the magnetic

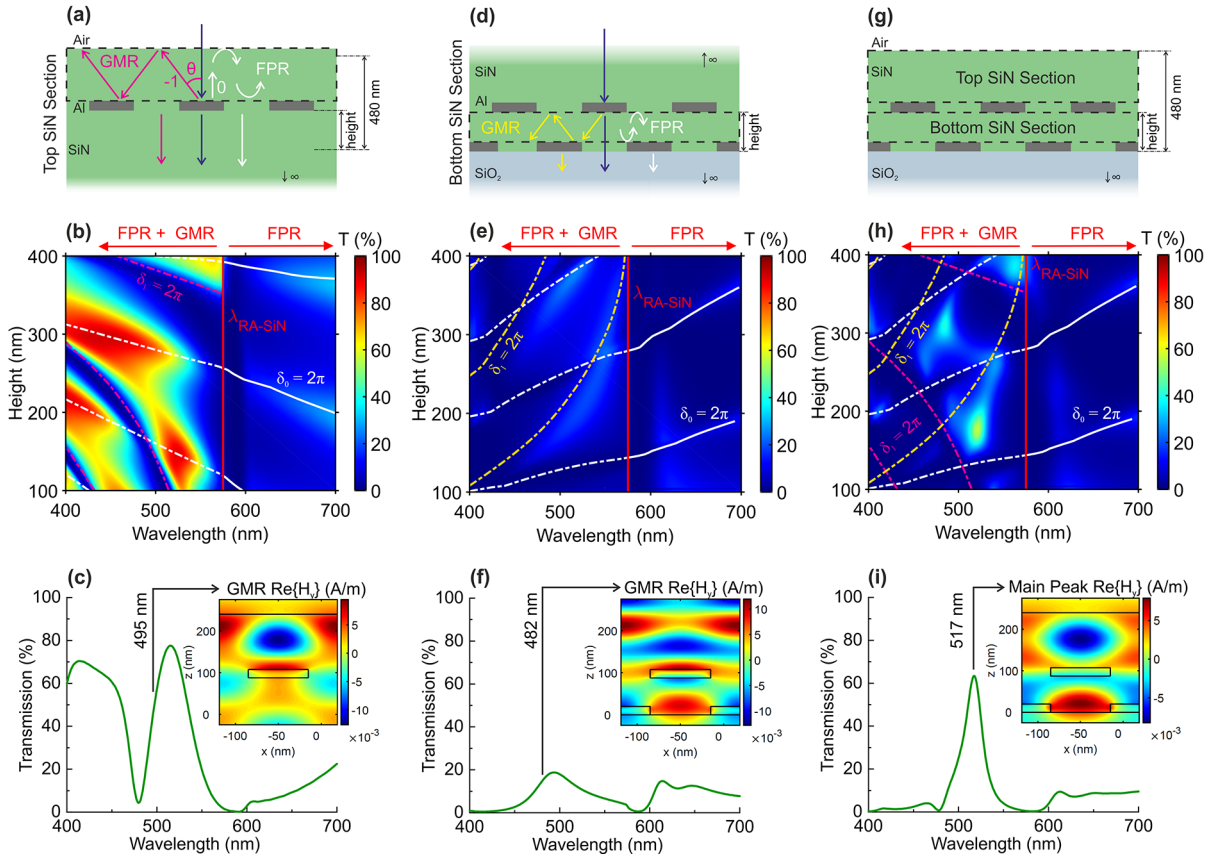

Figure 3. Investigating the transmission spectra of the SiN sections divided by the top grating. (a) The top SiN section delimited by the top metal grating and the SiN−air interface with (b) its transmission spectrum as a function of the height of the top grating with the red line indicating the Rayleigh anomaly $\lambda_{RA,SiN}$, white lines indicating FPRs, and magenta lines indicating GMRs. (c) Transmission spectrum of the top section for a grating height of 175 nm with the magnetic field Re{H_y} at λ_{GMR} shown in the inset. (d) The bottom SiN section delimited by the bottom and top metal grating with (e) its transmission spectrum as a function of the grating height. (f) The transmission spectrum of the bottom section for grating height 175 nm with the magnetic field Re{H_y} at λ_{GMR} shown in the inset. (g) The full structure as a combination of the top and bottom section with (h) its transmission spectrum as a function of the grating height. (i) The transmission spectrum of the full structure for a height of 175 nm with the magnetic field Re{H_y} and at the main transmission wavelength shown in the inset.

https://doi.org/10.1021/acsphotonics.1c01983
ACS Photonics XXXX, XXX, XXX−XXX

field $|H|^2$ at 419 nm shown in Figure 2a. The *asym* grating does not have the same dielectric interface at top and bottom, which leads to different SPP dispersion relations, meaning that SPPs cannot exist at both interfaces simultaneously and cannot propagate from one side to the other. There is only a broad transmission dip centered around $\lambda_{\text{SPP-SiO}_2}$. The presence of SPPs only at the bottom interface is confirmed by the magnetic field $|H|^2$ at 419 nm, shown in Figure 2b.

We can make a similar analysis for the gratings that have at least one Al−SiN interface: *symSiN* and *asym*. The Rayleigh anomaly $\lambda_{\text{RA-SiN}}$ now occurs at 574 nm, and the coupling of incident light to SPPs occurs at 597 nm. The redshift of these phenomena compared to the case of the Al−SiO_2 interface is caused by the higher refractive index of SiN. The condition for grating-assisted coupling of light to SPPs is met for $\lambda_{\text{SPP-SiN}}$ 612 nm. Again, we see a slight blueshift for our structure to 597 nm because at that wavelength the $\lambda/2$ condition is met for SPP standing waves on a single grating line. The EOT phenomenon explains the difference in line shape around the $\lambda_{\text{SPP-SiN}}$. The *symSiN* grating supports EOT and has a destructive and constructive interference complex centered around $\lambda_{\text{SPP-SiN}}$. The presence of SPPs at the top and bottom interface simultaneously is confirmed by the magnetic field $|H|^2$ at 597 nm, shown in Figure 2c. The *asym* grating does not support EOT and only has a broad transmission dip centered around $\lambda_{\text{SPP-SiN}}$. The presence of SPPs only at the top interface is confirmed by the magnetic field $|H|^2$ at 597 nm, shown in Figure 2d.

In summary, the substructures containing a single metal grating generally have transmission dips with a central wavelength determined by the grating pitch and the surrounding dielectric. Especially the *asym* grating is interesting, because it has two broad transmission dips, which is interesting for good out-of-band transmission suppression. We have chosen the pitch in such a way that the transmission dip of the Al−SiO_2 interface on the *asym* grating occurs at the violet end of the visible spectrum and that of the Al−SiN interface on the *asym* grating at the red end of the visible spectrum. These transmission dips set the edges of the spectral tuning range of the final design, meaning this range can be extended with a higher index contrast between the substrate and superstrate dielectrics.

Dielectric Sections Divided by the Top Metal Grating. Next, we aim to understand the transmission behavior of the SiN sections formed above and below the top metal grating.

The top SiN section is shown in Figure 3a, delimited by the top metal grating and the SiN−air interface. Figure 3b shows the transmission spectrum of the substructure as a function of the grating height. (We use the grating height and not the section height for an easier comparison with the other substructures.) This wavelength-height scan shows two wavelength regimes: one above the Rayleigh anomaly $\lambda_{\text{RA-SiN}}$, where light only has a zero-order diffraction mode, and one below $\lambda_{\text{RA-SiN}}$, where a first-order diffraction mode exists as well. The zero-order diffraction mode for normally incident light causes a FPR in the SiN section for specific wavelengths λ_{FPR}. At these wavelengths, the FP phase delay δ_0 of zero-order diffracted light accumulated on a single round-trip through the section equals a multiple of 2π:

$$\delta_0 = \frac{4\pi}{\lambda_{\text{FPR}}}(480\ \text{nm} - \text{height} - t_{\text{metal}}) + \phi_{r,\text{top}} = m\cdot 2\pi \tag{1}$$

In eq 1, m is an integer and $\phi_{r,\text{top}}$ is the phase shift upon zero-order reflection on the top grating for normally incident light. The FPRs are indicated in Figure 3b with white lines, they are present both below and above $\lambda_{\text{RA,SiN}}$. The first-order diffracted light that is reflected from the grating can couple to a leaky waveguide mode in the top SiN section for specific wavelengths λ_{GMR}. At these wavelengths, the phase delay δ_1 of first-order diffracted light accumulated on a single round-trip through the section equals a multiple of 2π:

$$\delta_1 = \frac{4\pi}{\lambda_{\text{GMR}}}(480\ \text{nm} - \text{height} - t_{\text{metal}})\cdot\cos(\theta) + \phi_{r,\text{top},\theta} = m\cdot 2\pi \tag{2}$$

In eq 2, $\phi_{r,\text{top},\theta}$ is the phase shift upon zero-order reflection for light incident with angle θ. The GMR can couple back to the zero-order mode upon transmission through the grating and will cause interference with the re-emitted light from the FPR on the transmission side. The FPR has a low finesse due to the low reflectivity of the SiN/air interface (10%) and the top grating (50% at 500 nm). The π phase change centered around the FPR is very broad, and the FP phase delay ϕ has an approximately linear course (see Supporting Information, S2). Interference of re-emitted light from the spectrally broad FPR and the spectrally narrow GMR leads to a characteristic Fano line shape[25] centered around λ_{GMR}. This line shape is visible in the transmission spectrum for a grating height of 175 nm, shown in Figure 3c. The magnetic field distribution Re{H_y} at λ_{GMR} is shown in the inset. In the wavelength-height scan in Figure 3b, we can now appreciate that, below the Rayleigh wavelength, the transmission maxima occur when there is constructive interference of the FPR and GMR, while above the Rayleigh wavelength, the transmission maxima coincide with the FPR wavelength.

We can analyze the bottom SiN section shown in Figure 3d in a similar way. Figure 3e shows the transmission spectrum of the substructure as a function of the top grating height. Again, this wavelength-height scan shows two wavelength regimes: one above the Rayleigh wavelength $\lambda_{\text{RA-SiN}}$ and one below. The condition for a FPR caused by zero-order diffracted light given in eq 1 is altered to

$$\delta_0 = \frac{4\pi}{\lambda_{\text{FPR}}}(480\ \text{nm} - \text{height} - t_{\text{metal}}) + \phi_{r,\text{bottom}} + \phi_{r,\text{top}} = m\cdot 2\pi \tag{3}$$

The term $\phi_{r,\text{bottom}}$ is added and is the phase shift upon zero-order reflection for normally incident light on the bottom grating. The condition for a GMR caused by first-order diffracted light transmitted through the top grating coupling into the bottom SiN section given in eq 2 is altered to

$$\delta_1 = \frac{4\pi}{\lambda_{\text{GMR}}}(480\ \text{nm} - \text{height} - t_{\text{metal}})\cdot\cos(\theta) + \phi_{r,\text{top},\theta} + \phi_{r,\text{bottom},\theta} = m\cdot 2\pi \tag{4}$$

The term $\phi_{r,\text{bottom},\theta}$ is added and is the phase shift upon zero-order reflection for incident light with angle θ on the bottom grating.

The finesse of the FPR in this bottom SiN section is considerably higher than that in the top section because of the higher reflectivity of the bottom grating (63% at 500 nm) compared to that of the top Al/air interface (12%). The π phase change centered around the FPR can be more clearly identified as a phase jump in the FP phase delay δ_0 (see Supporting Information, S2). In contrast to the FPR in the top SiN section, with its approximately linear FP phase delay, the

https://doi.org/10.1021/acsphotonics.1c01983
ACS Photonics XXXX, XXX, XXX−XXX

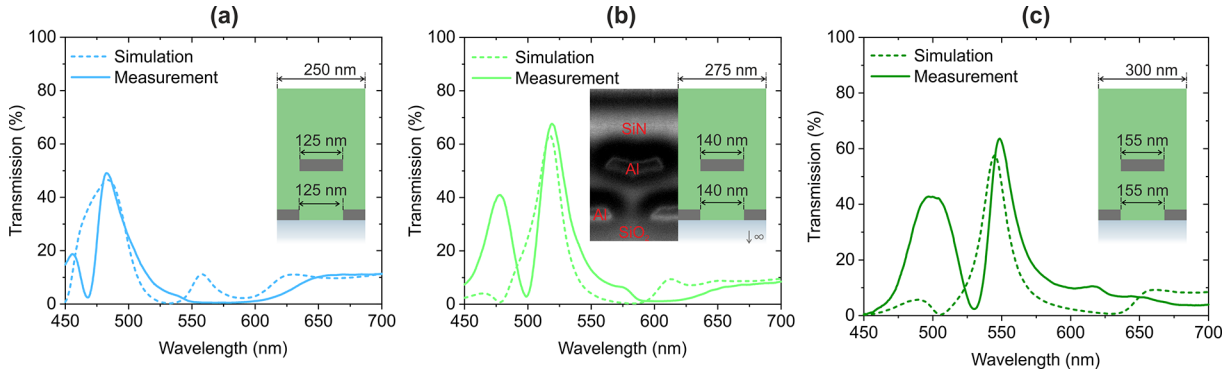

Figure 4. Measured (solid line) and simulated (dashed line) for the fabricated structures with (a) p = 250 nm, w_b = 125 nm, and w_t = 125 nm; (b) p = 275 nm, w_b = 140 nm, and w_t = 140 nm; (c) p = 300 nm, w_b = 155 nm, and w_t = 155 nm. The inset in (b) shows the SEM image of the cross-section of the fabricated structure.

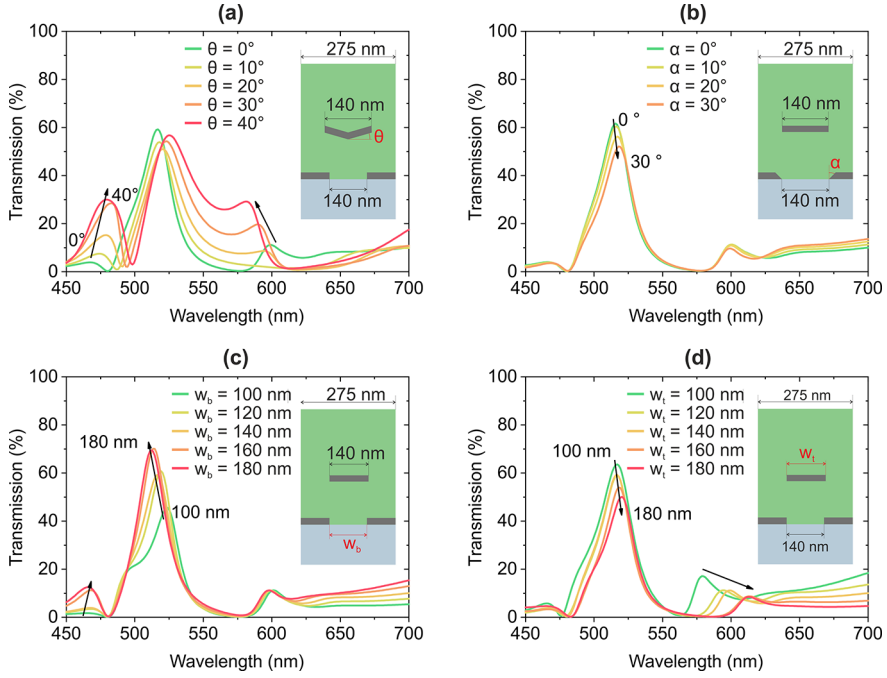

Figure 5. Investigation of key fabrication parameters of the filter structure using the transmission spectra with varying (a) top grating bend θ, (b) bottom grating sidewall slope α, (c) bottom grating gap w_b, and (d) top grating width w_t.

FPR in the bottom section gives rise to a more complex interference with the GMR that depends on the spectral detuning of the π phase jump of the FPR and GMR.[26] In the wavelength-height scan in Figure 3e, we can now appreciate that below the Rayleigh wavelength, transmission maxima occur when there is constructive interference of the FPR and the GMR, while above the Rayleigh wavelength, the transmission maximum coincides with the FPR wavelength.

Full Structure. Having investigated the plasmonic and dielectric resonances that occur in the top and bottom SiN sections, we can now merge the substructures to form the full structure, shown in Figure 3g. Figure 3h shows the transmission as a function of the top grating height, with the two wavelength regimes separated by the Rayleigh anomaly $\lambda_{RA\text{-}SiN}$ indicated. We have shown that destructive and constructive interference of FPRs and GMRs are responsible for the minima and maxima, respectively, in the transmission spectra for an individual section. Joining the top and bottom sections will lead to additional interference of light re-emitted from both sections. In the wavelength-height scan of the full structure in Figure 3h, we see an interesting area appear for grating heights around 175 nm: only one area of constructive interference remains in the transmission spectrum, around 525 nm. The transmission spectrum for grating height 175 nm is shown in Figure 3i with the inset showing the magnetic field $\mathrm{Re}\{H_y\}$ at the main transmission wavelength of 517 nm. We can observe the GMR magnetic field distributions in both the top and bottom SiN sections we had previously seen in the insets of Figure 3c and f for the separate sections. This is the central design we had introduced in Figure 1, in which we also showed that the location of this main transmission peak can be tuned by changing the grating pitch for a constant grating height and SiN slab thickness. The fwhm of the transmission band is only 20 nm, and its peak transmission is 63%, together with an excellent out-of-band suppression beyond what has been previously demonstrated for hybrid plasmonic−dielectric color filters with periodic structures. Our structures drastically outperform previously demonstrated plasmonic single-grating

https://doi.org/10.1021/acsphotonics.1c01983
ACS Photonics XXXX, XXX, XXX−XXX

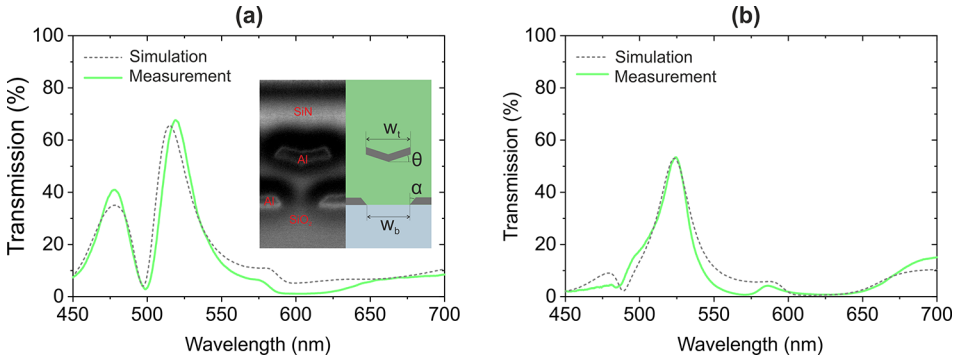

Figure 6. Improving the correspondence of simulation to measurement through adjustments in the key fabrication dimensions. (a) Measured and simulated transmission spectrum for the central design with adjusted dimensions in simulation (θ = 25°, α = 11°, w_b = 165 nm, and w_t = 125 nm). (b) Measured and simulated transmission spectrum for a design identical to the central design except for its smaller w_b, with adjusted dimensions in simulation (θ = 20°, α = 0°, w_b = 112 nm, and w_t = 125 nm).

structures with fwhms of 100 nm and a similar peak transmission.[27,28] The simulated transmission spectrum for the central design illuminated with the orthogonal polarization (see Supporting Information, S4) shows the filter functionality is not maintained, as expected for these grating structures. A logical expansion on this design is the use of two-dimensional gratings[29−32] to render the device polarization-independent. As our design requires the use of two gratings instead of one, as is commonly used in two-dimensional GMR filters, the free parameters in design are plenty and merit further investigation in themselves. For further investigation, the design we present can serve as a possible starting point.

EXPERIMENTAL RESULTS

Measured Transmission Spectra for Fabricated Structures and Effect of Geometric Fabrication Deviations. The measured and simulated transmission spectra for three different sets of pitch p, bottom width w_b, and top width w_t are shown in Figure 4. The spectral location and amplitude of the main transmission peak agree well between simulation and measurement for all three pitches. We observe an additional transmission peak at shorter wavelengths (between 450 and 500 nm) for all measurements. The measured transmission spectrum for the central design with illumination of orthogonal polarization can be found in Figure S4b of the Supporting Information. The inset of Figure 4b shows a SEM cross-section of the central design as fabricated. We see that the lateral dimensions and topology of the fabricated Al gratings deviate slightly from the design parameters. On the bottom grating a considerable sidewall slope is present. The top grating has a sunken center due to the lack of a chemical-mechanical polishing (CMP) step to level the SiN before the second Al layer is deposited.

To confirm that the additional transmission peak at shorter wavelengths is caused by the fabrication deviations in the lateral dimensions and topology of the grating, we perform a simulation study on how these affect the transmission spectrum: we look at the grating line widths w_b and w_t, the top grating sunken center, and the bottom grating sidewall slope. We investigate the transmission spectrum for the central design varying one of the dimensions at a time.

First, we give the top metal grating a V-shape with angle θ and a dip of 10 nm at the center to model the sunken center of the top grating. In the transmission spectra, shown in Figure 5a, we see that, for increasing θ, the small transmission peak caused by EOT around 600 nm on the top grating shifts to shorter wavelengths and merges with the main transmission peak to deteriorate its fwhm. Also, the additional transmission peak at shorter wavelengths increases considerably with increasing θ. This is because the dip caused by destructive interference of the GMR and the FPR, at 475 nm in the case of θ = 0°, is red-shifted up to 500 nm for θ = 40°. This means it moves further away from the dip associated with SPP absorption at the Al−SiO_2 interface on the bottom grating at 419 nm. Between these two dips, transmission is no longer suppressed and a transmission window opens, leading to the additional transmission peak centered around 475 nm.

Second, we model the bottom grating sidewall slope with the angle α, as shown in the inset of Figure 5b. For increasing α, the main transmission peak decreases slightly, but the rest of the spectrum is fairly unaffected by this sidewall slope.

Third, we look at the effect of changing w_b on the transmission spectrum. We see in Figure 5c that w_b affects two features: the main transmission peak at 517 nm and the additional transmission peak at shorter wavelengths. The main transmission peak decreases and acquires a shoulder on its blue side. The increased transmission at shorter wavelengths is due to the blue-shift of the transmission dip associated with SPPs at the Al−SiO_2 interface of the bottom grating when the Al lines become less wide and the $\lambda/2$ condition for SPP standing waves shifts to shorter wavelengths.

Finally, we look at the effect of changing w_t on the transmission spectrum shown in Figure 5d. We see that it affects two features in the spectrum: again the main transmission peak but now also the additional peak at longer wavelengths, caused by EOT through SPPs on the Al−SiN interface of the top grating. A larger w_t shifts the $\lambda/2$ condition for SPP standing waves to longer wavelengths, making the EOT redshift.

With the understanding of the qualitative effect of these four parameters on the transmission spectrum of the main design, we look for a set of parameters in the simulation that better fits the measurement for the main design. In Figure 6a, we show the measured transmission spectrum for the central design, together with the simulated spectrum now with altered values for the four parameters: θ = 25°, α = 11°, w_b = 165 nm, and w_t = 125 nm. The agreement between measurement and simulation is strongly improved. Although we can already conclude that a CMP step is necessary before the deposition of the second Al layer to ensure there is no sunken center on the

https://doi.org/10.1021/acsphotonics.1c01983
ACS Photonics XXXX, XXX, XXX−XXX

top Al grating from Figure 5a, there is an interesting side note to be made from Figure 5c: a sufficiently small w_b can suppress the additional transmission peak at short wavelengths caused by the sunken center of the top grating. A smaller w_b leads to a redshift of the SPP transmission dip as the Al lines become wider and the transmission window is closed again. Figure 6b shows the measured transmission spectrum for a CF with the same dimensions as the central design, but now with a smaller w_b (112 nm). We find that the best fit between measurement and simulation occurs for a similar θ (20° in this case). Both simulation and measurement confirm that a smaller w_b does indeed reduce the additional transmission peak with only a small penalty in the main peak transmission, still achieving a fwhm of 25 nm and a peak transmission of 53%.

CONCLUSIONS

We have experimentally demonstrated a novel transmission color filter device with a fwhm of 25 nm for a peak transmission of 53%, effectively halving the fwhm of the state-of-the-art periodically structured plasmonic−dielectric color filters, for the same peak transmission. We have used a simulation study to illustrate the working principle of the filter and the main design considerations. The study also shows a possible gain in performance to a fwhm of 20 nm and peak transmission over 60% if the topology of the top grating is better controlled during fabrication. This could be achieved with an additional CMP step before the deposition and patterning of the top grating, a step that was not yet included in the fabrication process of the characterized filters. We have demonstrated that the small fwhm is explained by the nature of the main transmission peak; it is a constructive interference of FPRs and GMRs occurring both above and below the top metal grating, which effectively splits the full SiN slab height up in two dielectric sections. We have shown that the excellent out-of-band suppression at shorter and longer wavelengths is caused by propagating SPPs that effectively set the width of the filter stopband and the edges of the spectral tuning range. The width and location of these stopbands can be tuned by changing the width of the metal grating line, without needing to change the pitch. The filter works for light polarized perpendicular to the metal grating lines because the grating's first order diffraction mode is necessary to establish a GMR. To render this design polarization independent in future research, we propose moving from a one-dimensional grating to a two-dimensional grating, previously demonstrated to establish polarization-independent GMRs. Although a fwhm penalty can be expected for this transition, we will further pursue it since we believe the excellent out-of-band suppression and exceptionally low fwhm of our design compared to other plasmonic grating filters make the investigation worthwhile.

The design can be altered to achieve filters in different wavelength regions and with materials with different optical properties. The strongly reduced fwhm of this hybrid plasmonic−dielectric CF can further push the spectral resolution for multispectral imaging applications at a significantly lower fabrication cost than the current all-dielectric thin-film CFs. We believe this novel design can facilitate many other on-chip spectral imaging applications due to its limited thickness and easy monolithic integration with full CMOS compatibility.

METHODS

Analytical Formulas for the Rayleigh Anomaly and the Surface Plasmon Polariton. The Rayleigh anomaly occurs where the grating diffraction reaches 90° and the relation of the grating pitch p, substrate refractive index n_{sub}, and its wavelength λ_{RA} is given by

$$p = m\frac{\lambda_{RA}}{n_{sub}} \text{ with } m = 1, 2, 3, \ldots \tag{5}$$

The phase-matching condition for normally incident light to couple to propagating SPPs in a grating with pitch p at wavelength λ_{SPP} for the first order is given by

$$p = m\cdot\lambda_{SPP}\sqrt{\frac{\epsilon_m + \epsilon_d}{\epsilon_m\cdot\epsilon_d}} \text{ with } m = 1, 2, 3, \ldots \tag{6}$$

FDTD Simulations. The simulations are done with the FDTD solver from Lumerical. The simulation includes periodic boundary conditions, a normally incident plane wave source for the visible wavelength range, and a source polarization orthogonal to the metal grating lines. The dielectric function of Al is extracted from ellipsometry measurements on previously deposited Al test blanket wafers. The SiO_2 dielectric function is taken from the literature.[33] In the simulation study, the SiN refractive index was fixed at 2.09 (and the extinction coefficient at 0), and in the Experimental Results, the refractive index extracted from ellipsometry measurements (see Supporting Information, S5) was used for better agreement in the corresponding simulations.

Fabrication. The color filters are fabricated on a 200 mm quartz wafer (775 μm thick) in a CMOS pilot line, with each individual color filter design spanning 280 × 280 μm^2. Such large filter areas were chosen to facilitate the measurements. After a cleaning step, the first 40 nm Al layer is deposited with physical vapor deposition (PVD). This Al layer is patterned with optical lithography and etched down to the SiO_2 substrate with an inductive-coupled plasma-reactive ion-etch process. Photoresist is used as the etch mask. On top of the patterned grating, a 175 nm thick layer of SiN was deposited with plasma-enhanced chemical vapor deposition (PECVD). Then, the top 40 nm Al layer is deposited and patterned with the same lithography and etch processes used for the bottom Al layer. A 400 nm SiN layer is deposited with PECVD, on which a chemical-mechanical polishing (CMP) step is used to flatten the top surface of the sample. An additional PECVD SiN layer is deposited to ensure the top SiN layer is 265 nm thick, as designed.

Transmission Measurements. The color filters were measured with a custom-built transmission spectroscopy setup. Samples were illuminated with a collimated LED white light source. On the transmission side, a 10× objective with NA 0.28 was used to collect the transmitted light. The light was then split with a polarizing beam splitter between a CMOS camera and a wide-range CCD spectrometer, with the desired polarization sent to the spectrometer and the unwanted polarization to the CMOS camera for sample inspection.

ASSOCIATED CONTENT

Supporting Information

The Supporting Information is available free of charge at https://pubs.acs.org/doi/10.1021/acsphotonics.1c01983.

https://doi.org/10.1021/acsphotonics.1c01983
ACS Photonics XXXX, XXX, XXX−XXX

Table with dimensions of optimized unit cell designs for different pitches; Transfer matrix method applied to separate SiN sections to isolate Fabry-Pérot resonances; Simulated and measured transmission spectra for the orthogonal polarization (electric field parallel with the grating lines); Simulated transmission spectra for nonzero angle of incidence; Refractive index and extinction coefficient extracted from ellipsometry measurement (PDF)

AUTHOR INFORMATION

Corresponding Author

Anabel De Proft − *Department of Physics and Astronomy, KU Leuven, 3001 Leuven, Belgium; IMEC, 3001 Leuven, Belgium;* orcid.org/0000-0002-0329-7589; Email: anabel.deproft@imec.be

Authors

Kristof Lodewijks − *IMEC, 3001 Leuven, Belgium*

Bruno Figeys − *IMEC, 3001 Leuven, Belgium*

Dmitry Kouznetsov − *Department of Physics and Astronomy, KU Leuven, 3001 Leuven, Belgium; IMEC, 3001 Leuven, Belgium;* orcid.org/0000-0001-8440-742X

Niels Verellen − *Department of Physics and Astronomy, KU Leuven, 3001 Leuven, Belgium; IMEC, 3001 Leuven, Belgium*

Nga P. Pham − *IMEC, 3001 Leuven, Belgium*

Bart Vereecke − *IMEC, 3001 Leuven, Belgium*

Deniz Sabuncuoglu Tezcan − *IMEC, 3001 Leuven, Belgium*

Roelof Jansen − *IMEC, 3001 Leuven, Belgium*

Pol Van Dorpe − *Department of Physics and Astronomy, KU Leuven, 3001 Leuven, Belgium; IMEC, 3001 Leuven, Belgium*

Xavier Rottenberg − *IMEC, 3001 Leuven, Belgium*

Complete contact information is available at: https://pubs.acs.org/10.1021/acsphotonics.1c01983

Notes

The authors declare no competing financial interest.

REFERENCES

(1) Lapray, P.-J.; Wang, X.; Thomas, J.-B.; Gouton, P. Multispectral Filter Arrays: Recent Advances and Practical Implementation. *Sensors* **2014**, *14*, 21626−21659.

(2) Shaw, G. A.; Burke, H.-h. K. Spectral Imaging for Remote Sensing. *Lincoln Laboratory Journal* **2003**, *14*, 3−28.

(3) Chen, Y.-R.; Chao, K.; Kim, M. S. Machine vision technology for agricultural applications. *Comput. Electron. Agric.* **2002**, *36*, 173−191.

(4) Li, Q.; He, X.; Wang, Y.; Liu, H.; Xu, D.; Guo, F. Review of spectral imaging technology in biomedical engineering: achievements and challenges. *J. Biomed. Opt* **2013**, *18*, 100901.

(5) Tack, N.; Lambrechts, A.; Soussan, P.; Haspeslagh, L. A compact, high-speed, and low-cost hyperspectral imager. *Proc. SPIE* **2012**, *8266*, 82660Q.

(6) Geelen, B.; Tack, N.; Lambrechts, A. A compact snapshot multispectral imager with a monolithically integrated per-pixel filter mosaic. *Proc. SPIE* **2014**, 89740L.

(7) Chen, Q.; Hu, X.; Wen, L.; Yu, Y.; Cumming, D. R. S. Nanophotonic Image Sensors. *Small* **2016**, *12*, 4922−4935.

(8) Xu, T.; Shi, H.; Wu, Y.-K.; Kaplan, A. F.; Ok, J. G.; Guo, L. J. Structural Colors: From Plasmonic to Carbon Nanostructures. *Small* **2011**, *7*, 3128−3136.

(9) Yu, Y.; Wen, L.; Song, S.; Chen, Q. Transmissive/Reflective Structural Color Filters: Theory and Applications. *J. Nanomater.* **2014**, *2014*, 1−17.

(10) Kristensen, A.; Yang, J. K. W.; Bozhevolnyi, S. I.; Link, S.; Nordlander, P.; Halas, N. J.; Mortensen, N. A. Plasmonic colour generation. *Nat. Rev. Mater.* **2017**, *2*, 16088.

(11) Maier, S. A. *Plasmonics: Fundamentals and Applications*; Springer US: New York, 2007; pp 39−52.

(12) Ebbesen, T. W.; Lezec, H. J.; Ghaemi, H. F.; Thio, T.; Wolff, P. A. Extraordinary optical transmission through sub-wavelength hole arrays. *Nature* **1998**, *391*, 667−669.

(13) Chen, Q.; Das, D.; Chitnis, D.; Walls, K.; Drysdale, T. D.; Collins, S.; Cumming, D. R. S. A CMOS Image Sensor Integrated with Plasmonic Colour Filters. *Plasmonics* **2012**, *7*, 695−699.

(14) Lee, H.-S.; Yoon, Y.-T.; Lee, S.-S.; Kim, S.-H.; Lee, K.-D. Color filter based on a subwavelength patterned metal grating. *Opt. Express* **2007**, *15*, 15457−15463.

(15) Catrysse, P. B.; Wandell, B. A. Integrated color pixels in 0.18-μm complementary metal oxide semiconductor technology. *J. Opt. Soc. Am. A* **2003**, *20*, 2293−2306.

(16) Yokogawa, S.; Burgos, S. P.; Atwater, H. A. Plasmonic Color Filters for CMOS Image Sensor Applications. *Nano Lett.* **2012**, *12*, 4349−4354.

(17) Shah, Y. D.; Connolly, P. W. R.; Grant, J. P.; Hao, D.; Accarino, C.; Ren, X.; Kenney, M.; Annese, V.; Rew, K. G.; Greener, Z. M.; Altmann, Y.; Faccio, D.; Buller, G. S.; Cumming, D. R. S. Ultralow-light-level color image reconstruction using high-efficiency plasmonic metasurface mosaic filters. *Optica* **2020**, *7*, 632.

(18) Fleischman, D.; Sweatlock, L. A.; Murakami, H.; Atwater, H. Hyper-selective plasmonic color filters. *Opt. Express* **2017**, *25*, 27386.

(19) He, X.; Liu, Y.; Ganesan, K.; Ahnood, A.; Beckett, P.; Eftekhari, F.; Smith, D.; Uddin, M. H.; Skafidas, E.; Nirmalathas, A.; Unnithan, R. R. A single sensor based multispectral imaging camera using a narrow spectral band color mosaic integrated on the monochrome CMOS image sensor. *APL Photonics* **2020**, *5*, 046104.

(20) Pinton, N.; Grant, J.; Collins, S.; Cumming, D. R. S. Exploitation of Magnetic Dipole Resonances in Metal−Insulator−Metal Plasmonic Nanostructures to Selectively Filter Visible Light. *ACS Photonics* **2018**, *5*, 1250−1261.

(21) Rosenblatt, D.; Sharon, A.; Friesem, A. Resonant grating waveguide structures. *IEEE J. Quantum Electron.* **1997**, *33*, 2038−2059.

(22) Tibuleac, S.; Magnusson, R. Reflection and transmission guided-mode resonance filters. *J. Opt. Soc. Am. A* **1997**, *14*, 1617−1626.

(23) Wang, S. S.; Magnusson, R. Multilayer waveguide-grating filters. *Appl. Opt.* **1995**, *34*, 2414−2420.

(24) Uddin, M. J.; Magnusson, R. Efficient Guided-Mode-Resonant Tunable Color Filters. *IEEE Photonics Technol. Lett.* **2012**, *24*, 1552−1554.

(25) Limonov, M. F.; Rybin, M. V.; Poddubny, A. N.; Kivshar, Y. S. Fano resonances in photonics. *Nature Photon* **2017**, *11*, 543−554.

(26) Fang, Y.; Ruan, Z. *Fano Resonances in Optics and Microwaves*; Springer: Cham, 2018; pp 157−183.

(27) Xu, T.; Wu, Y.-K.; Luo, X.; Guo, L. J. Plasmonic nanoresonators for high-resolution colour filtering and spectral imaging. *Nat. Commun.* **2010**, *1*, 1−5.

(28) Zeng, B.; Gao, Y.; Bartoli, F. J. Ultrathin Nanostructured Metals for Highly Transmissive Plasmonic Subtractive Color Filters. *Sci. Rep.* **2013**, *3*, 1−9.

(29) Peng, S.; Morris, G. M. Experimental demonstration of resonant anomalies in diffraction from two-dimensional gratings. *Opt. Lett.* **1996**, *21*, 549−551.

(30) Boonruang, S.; Greenwell, A.; Moharam, M. G. Multiline two-dimensional guided-mode resonant filters. *Appl. Opt.* **2006**, *45*, 5740−5747.

(31) Peters, D. W.; Boye, R. R.; Wendt, J. R.; Kellogg, R. A.; Kemme, S. A.; Carter, T. R.; Samora, S. Demonstration of polarization-independent resonant subwavelength grating filter arrays. *Opt. Lett.* **2010**, *35*, 3201−3203.

(32) Ferraro, A.; Zografopoulos, D. C.; Caputo, R.; Beccherelli, R. Guided-mode resonant narrowband terahertz filtering by periodic

metallic stripe and patch arrays on cyclo-olefin substrates. *Sci. Rep.* **2018**, *8*, 17272.
(33) Palik, E. D. *Handbook of Optical Constants of Solids*; Academic Press, 1998.

https://doi.org/10.1021/acsphotonics.1c01983
ACS Photonics XXXX, XXX, XXX−XXX